

1

Part I

2

Theory introduction

³ Chapter **1**

⁴ **Standart model**

⁵ Chapter **2**

⁶ **Theory of pp collisions**

⁷ Chapter **3**

⁸ **PDF fits and DLGAP formalism**

⁹ Chapter **4**

¹⁰ **Physics of WZ bosons**

¹¹ **4.1 Theory**

¹² **4.2 Cross-section measurement**

13

Part II

14

Experimental setup

15

Chapter **5**

16

LHC

¹⁷

Chapter

6

¹⁸

ATLAS experiment

19

Chapter

7

20

Software

22 Monte Carlo

23 The Monte Carlo(MC) method was invented by scientists working on the atomic bomb in the 1940s.
 24 Its core idea is to use random samples of parameters or inputs to explore the behavior of a complex
 25 system or process. Nowadays, MC are essential part of both theoretical and experimental particle
 26 physics research. This chapter gives an overview of ATLAS experiment simulation scheme, simulation
 27 methods and software used. Also, a techniques for fast simulation will be discussed.

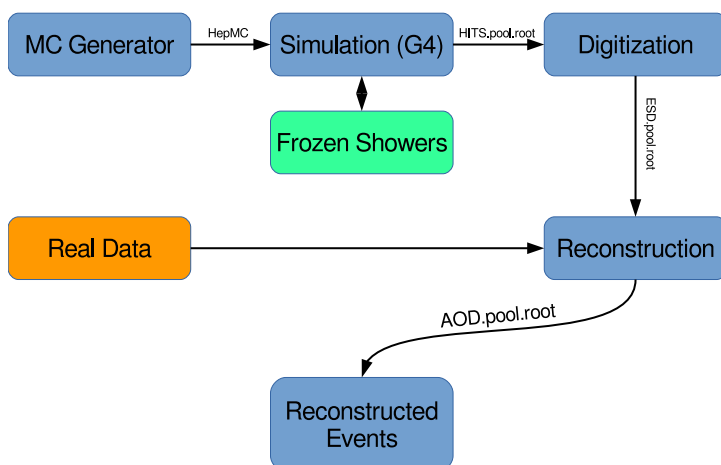
28 **8.1 Monte Carlo simulation at ATLAS experiment**

Fig. 8.1: Diagram of the ATLAS MC production chain

29 MC is allowing to make different analysis, such as compare data with predictions, study detector
 30 or selection algorithms performance. All of this applications are requiring MC precision. Simulation
 31 software expects to use precise physics models for sampling and have large enough statistics, to
 32 exclude statistical uncertainties (usually 5 times more, than expected in a data). ATLAS simulation
 33 software is integrated into Athena and usually used during large production of events. Simulation
 34 chain is generally divided into 4 main steps (Figure 8.1):

35 **Event generation** Simulation of hard interaction and a resulting high-energy particles parameters.
 36 This step is independent of ATLAS detector geometry.

37 **Simulation** Simulation of energy depositions ("hits") done by final state particles in ATLAS detector.

38 **Digitalization** Simulation of detector response using "hits" information: first, inputs to the read out
 39 drivers (ROD's), called "digits" are constructed, then, ROD functionality is emulated. Detector
 40 noise effects are added at this stage.

41 **Reconstruction** Production of the Analysis Object Data (AOD) files, which are containing sufficient
 42 information for physics analysis. This stage is identical for both data and MC

43 This scheme allows to use computing resources more efficiently, than with a single-step simulation,
 44 and simplifies software validation, since it is possible to reuse files from previous stages. In the
 45 following sections event generation and simulation will be described in more details

46 **8.1.1 Event generators**

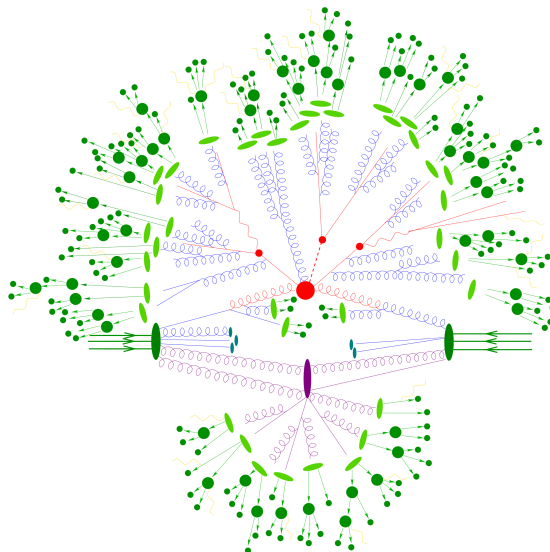


Fig. 8.2: Schematic view of a $t\bar{t}H$ event produced in a pp -collision: the hard scattering is shown as a red blob with the solid and dashed lines as the resulting three particles. Independently happening multi-particle interactions are indicated by the violet blob. Parton showers are shown with curly lines. Hadronization yields hadrons as shown in light green, while the final state particle are dark green.

47 The outcome of the hard interaction could be simple scattering of the hadron elementary con-
 48 stituents, their annihilation into new resonances or a combination of two. In any case, the final state
 49 has a large particles multiplicity. The main goal of event generator is to provide a complete picture of
 50 this final states: description of the particle types and momentia on event-by-event basis. The fac-
 51 torisation theorem [?] allows to make event generation in independent stages, which are dominated
 52 by different dynamics:

53 **Modelling of hard subprocess** Hard subprocess is happening at the smallest scales of times and
 54 distance, where all of the colliding partons are considered free. Process of interest is simulated
 55 by selecting production channels and calculating corresponding matrix elements (ME) in the
 56 desired level of accuracy in perturbation theory . Most of the generators have leading order
 57 or next to leading order ME in α_s .

58 **Parton showering** Quarks and gluons from hard process can radiate secondary quarks and gluons,
59 resulting on the dozens of additional partons associated with the event. This process calculated
60 as step-by-step evolution of momentum transfer scales from highest (hard subprocess), to
61 the lowest (around 1 GeV). There is a possibility of double counting between showers and hard
62 subprocess. This can be avoided using matching approach, for which higher order corrections
63 to ME are integrated with parton showers, or merging strategy, where jet resolution scale is
64 used as a threshold between matrix elements and parton showers.

65 **Hadronisation** Final stable color-neutral particles, what can be detected in experiment, are formed
66 during hadronisation. This occurs at larger nonperturbative scales and usually implemented
67 using different phenomenological models.

68 **Modelling underlying event** Parallel to the main process other collisions of partons can occur,
69 called underlying event. These additional interaction can produce partons which contribute to
70 the final state. This is one of the least understood aspect of hadronic collisions.

71 Schematic plan of simulation of ttbar event is shown in Figure ???. The hard scattering itself is shown
72 as a red blob with the solid and dashed lines indicating the resulting particles, which themselves decay
73 further. Underlying event is indicated by the violet blob. Parton showers are shown with curly lines.
74 Hadronization yields hadrons as shown in light green, while the final state particles are dark green.
75 The current analysis uses samples generated with the following generators:

76 Powheg [?] Powheg is generator with NLO ME [?], that can be interfaced with other generator(such
77 as Pythia or Herwig) for higher precision of showering.

78 Pythia [?] Pythia is a general purpose generator for hadronic, hadron-lepton and leptonic collisions.
79 It can model initial and final state showers, hadronisation and decays, underlying event (via
80 multi parton interactions). Pythia contains library with around 240 processes with LO ME. It
81 uses Lund String model [?] for hadronisation.

82 Herwig [?] Herwig is a LO general purpose event generator for simulation lepton-lepton, hadron-
83 lepton and hadron-hadron collisions. The main difference between Pythia and Herwig is that
84 it uses angular ordering in the parton showers and also models the hadronisation step based
85 on the cluster fragmentation

86 Sherpa [?] Sherpa is a generator with tree level of matrix elements, featuring its own implementation
87 of parton shower and hadronisation models.

88 Photos [?] Precision tool for QED radiative corrections in W and Z decays.

89 Tauola [?] Generator, used to describe leptonic and semi-leptonic τ -decays.

90 8.1.2 Simulation in Geant4

91 After event generation, simulation software obtains hardware response for final state particles. The
92 main method used by ATLAS, referred to as *Full Simulation*, makes use of the Geant4 [?]. It is C++
93 based toolkit for the simulation of the passage of particles through matter. It is used in a wide range
94 of experiments in high energy and nuclear physics.

95 Geant4 can simulate complex detector structures with sensitive detector material and correspond-
96 ing infrastructure. It can also calculate basic properties of materials, like radiation and interaction

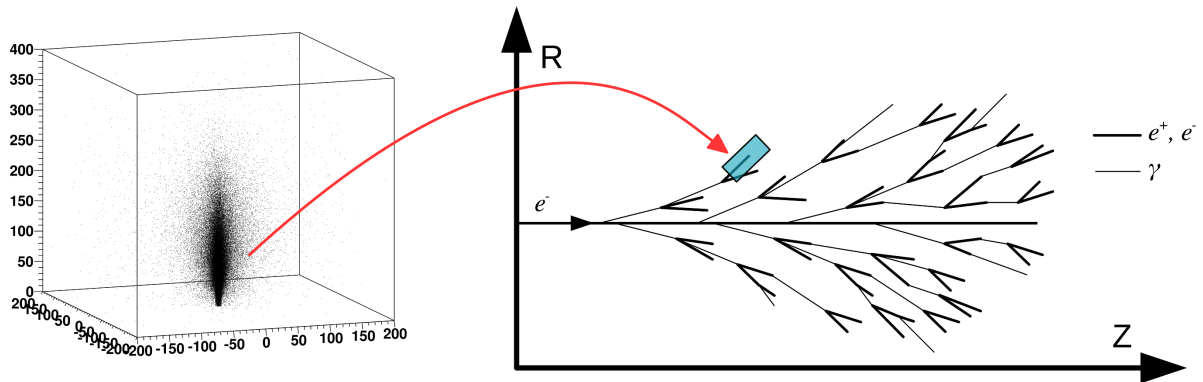


Fig. 8.3: Diagram showing the shower substitution of the low-energy particle, during the high-energy particle simulation.

length. For detector Geant4 stores "hits" information - snapshots of physical interactions. In Geant4 events and particles are simulated separately and each particle is moved step by step. Size of this step is chosen to preserve both CPU performance and required precision. Physics is treated as a set of discrete processes. They could be handled either at rest, along step or after it. Geant4 package has different models and approximations for hadronic and electromagnetic processes. Some of them are not approximate, but computationally fast. It allows to choose set of the models, called physics list, depending on particular requirements. There are several reference physics lists, that are validated for each new release of Geant4 software. ATLAS experiment is using one of this lists.

It is necessary to have mass MC production for each data taking, what is taking most of the resources. Uncertainties of some of Run-I analyses are dominated by available MC statistics.

It is possible to improve in CPU usage by tuning physics list or working on a magnetic field parametrisation. Also there are long term developments for multi-threading and vectorisation of the code. Yet, Run-2 has a higher pileup and luminosity, so even more MC events are needed. This means that fast and accurate simulation approach is essential. During simulation largest time is spent on calorimeters. This is the motivation for development of fast calorimetry techniques.

There are two main methods used in ATLAS:

- Parametrisation of calorimeter cells response. Spacial energy response is simulated using longitudinal and lateral energy profiles.
- Frozen Showers. This technique will be described more detailed in the following section

8.1.3 Frozen Showers

Main principle of this method is described by its name. It is using pre-simulated "frozen" showers generated in full simulation and stored in a library. Particles below minimum energy thresholds are killed and replaced with these showers. All of the other particles are simulated using full simulation. This process is schematically shown in a Figure 8.3.

The library itself organized as follows: the header contains basic simulation parameters, like Geant4, geometry and ATLAS software release version and physics list used. Showers are stored in a bins of positional variables (see sec. 8.1.3), while energy remain unbinned. Each shower stores lateral and transverse size and information about energy, time and positions of the hits.

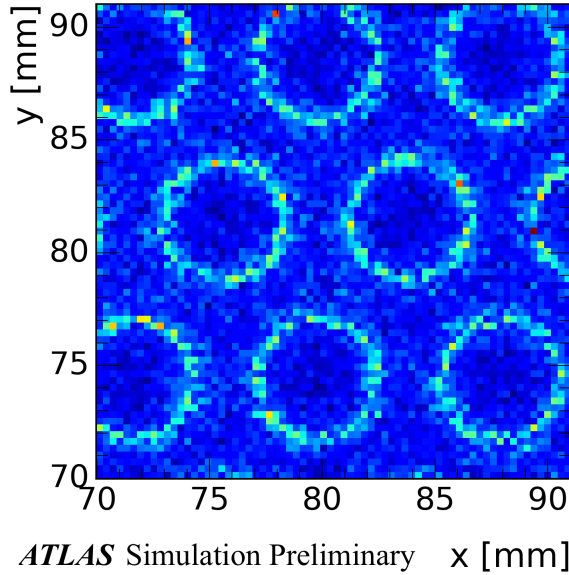


Fig. 8.4: Average energy response in a calorimeter vs x,y for electrons with energy less than 1 GeV

125 Production use of Frozen Showers

126 During simulation, if an energy of a particle falls below cut-off energy, the particle algorithm examines
 127 resulting shower containment. It checks that particle is far from the edges of calorimeter, so what
 128 shower will be by 90% inside calorimeter. This depends also on a energy of particle, because
 129 shower sizes are growing with energy. When particle is removed and substituted by shower taken
 130 from corresponding eta and distance bin with the closest energy found. Energies of the hits in shower
 131 found are scaled to fully correspond to particle energy. Additionally, shower direction is changed to
 132 the direction of the particle.

Frozen Showers have been used in ATLAS Monte-Carlo production since run-1. This method is applicable for all LAr calorimeters in ATLAS, but currently it is enabled for simulation of forward calorimeters (FCAL), since it is showing the smallest differences, compared to the other fast simulation methods (e.g parametrisation). This is because of large of non-uniformly distributed sensitive material, which is giving different responce, than a dead material (Figure 8.5). Resolution of a calorimeter can be written as:

$$\frac{\sigma}{E} \approx \frac{1}{\sqrt{E}} \oplus \frac{1}{E} \oplus const, \quad (8.1)$$

where symbol \oplus indicates a quadratic sum. The first term is 'stochastic term', which includes intrinsic shower fluctuations, second takes into account readout noise effects and pile-up fluctuations. Constant term derives from non-uniformities in a detector, what are causing large fluctuation of the energy loss. Resolution of high-energy electrons is mostly dominated by this term. Example of these fluctuations is shown on a Figure 8.4. Circles are corresponding to a LAr gaps inside FCAL. It can be seen, that particles inside sensitive material are having more energetic showers, than particles in a dead material. It is possible to capture this structure by introducing distance to a closest rod center:

$$D = \min(\sqrt{dx^2 + dy^2}, \sqrt{(step_x - dx)^2 + dy^2}, \sqrt{(step_x/2 - dx)^2 - (step_y - dy)^2}), \quad (8.2)$$

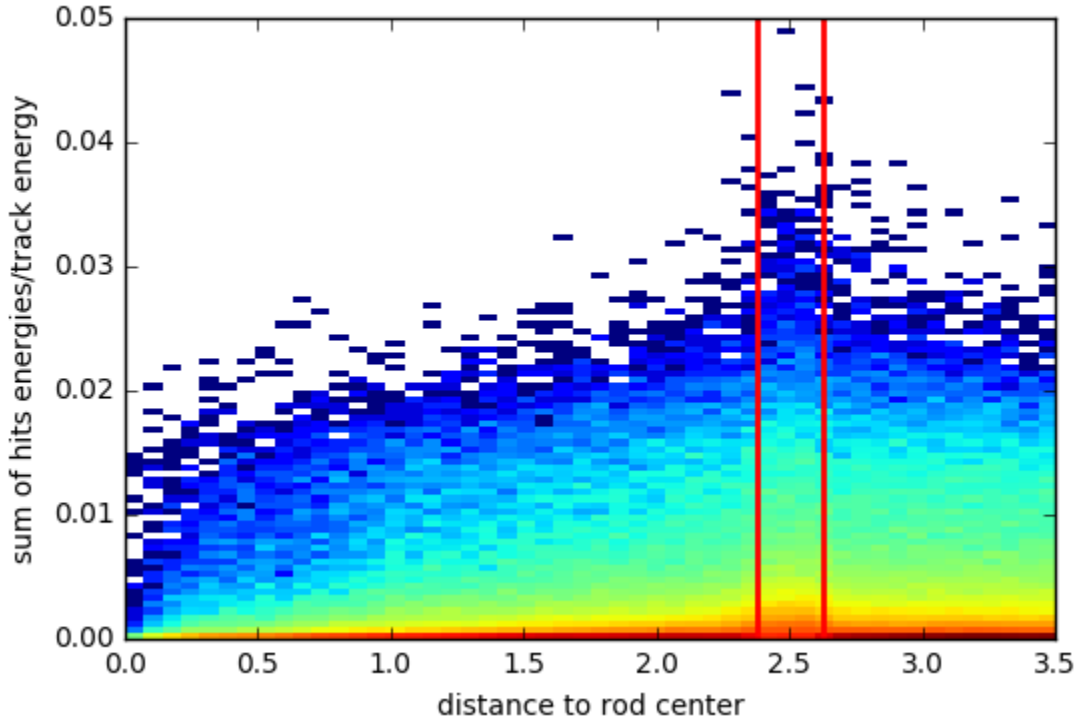


Fig. 8.5: Energy response for electrons in a calorimeter for all electrons in a library

where dx and dy are the distances to a rod center in a x and y plane respectively. They are calculated as:

$$dy = y - n[] \quad (8.3)$$

Dependency of summed energy of shower on the distance defined above is shown on a Figure 8.5. Gap is marked by the red lines. Size of this differences between sensitive material and dead material depends on a initial particle momentia (Figure 8.6 a and b). For electrons with energy greater than 500 GeV they are almost negligible. Additionally, at higher energies gain in a CPU time is moderate, while library becomes bigger. This is reason for an upper limit to be set at 1000 MeV

Performance of frozen showers is also depending on a lower limit of a method. Distribution of shower energies, used for production of high-energetic electron (1000 GeV in that case), is shown on a Figure . More than 50% of them are having energy less than 20 MeV. Studies have showed, that Frozen showers are slower, than a standard Geant4 simulation for showers with energy 3 MeV. This is happening due to library non-binned structure for energy. This makes search of closest energy shower in a library slower, than simulation of shower with zero or one hit in a sensitive detector.

144 **Generation of Frozen Showers library**

145 In a Frozen Shower method there are separate libraries for each particle and subdetector used.
146 Showers should cover fully energy and pseudorapidity region and be able to describe data, that is

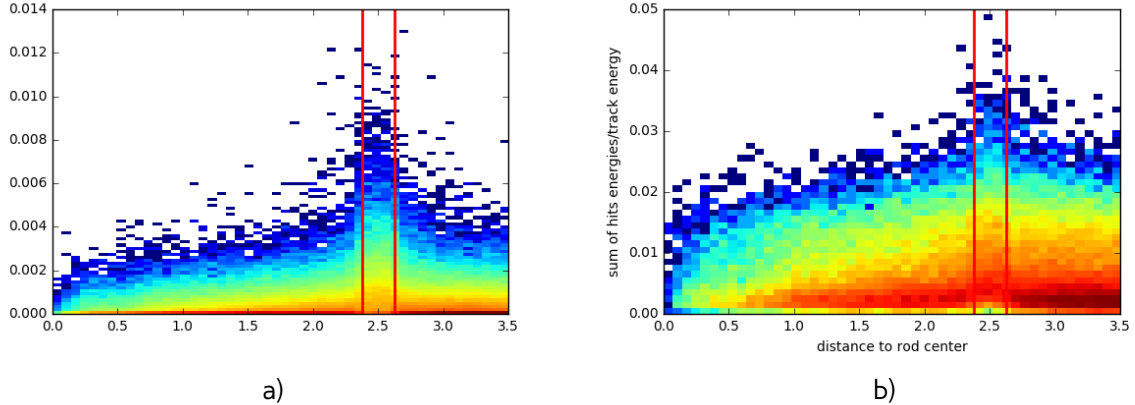


Fig. 8.6: Energy response for electrons in a calorimeter for a) electrons with energy less than 100 MeV b) electrons with energy bigger, than 100 MeV

The general frozen showers parameters	
Detectors used	FCAL1, FCAL2, FCAL3
Type of the particle	photons, electrons, neutrons
Energy range	$E_\gamma < 10 \text{ MeV}$, $E_e < 1000 \text{ MeV}$, $T_n < 100 \text{ MeV}$
Containment requirement	$\Delta E_{\text{shower}} > 98\%$
The library post-processing parameters	
Generation clustering cutoff	$(\Delta R_{\text{cluster}})^2 < 25 \text{ mm}$
Generation truncation cutoff	$R_{\text{hit}}^2 < 50000 \text{ mm}$, $\Delta E_{\text{shower}} < 1\%$

Table 8.1: Main parameters used for the frozen shower libraries in FCAL

needed during simulation. This is why 2 stages simulation approach have been used. The first stage takes initial particle parameters from a physical processes (ttbar or a single electron).

The first stage is to take initial particle parameters, that later will be used in a library from a physical process. This is done using simulation of some process (e.g. ttbar or single electron). Every time, when particle becomes eligible for Frozen Showers, it parameters are saved in a HepMC format. Particles inside calorimeter tend to cluster tightly around initial track, so random truncation of initial particles is used to obtain better detector coverage. On the second stage, this primary particles are propagated through the calorimeter using standart Atlas simulation infrastructure. Resulted shower parameters are saved in a library. This procedure allows to take into account sampling fluctuations and charge-collection effects on a hit information automatically. Additionally, in order to save disc space as well as a memory consumption, hit information is compressed. This compression is done in a two steps, hit merging and truncation:

- if the distance between any two hits is smaller, than a given parameter R_{\min} , then hits are merged into one deposit at the energy weighted center of them. This process is done iteratively.
- hits whose energies are below the fraction f of the total energy sum of all hits, are truncated. The energy of remaining hits is rescaled back to preserve the total deposited energy.

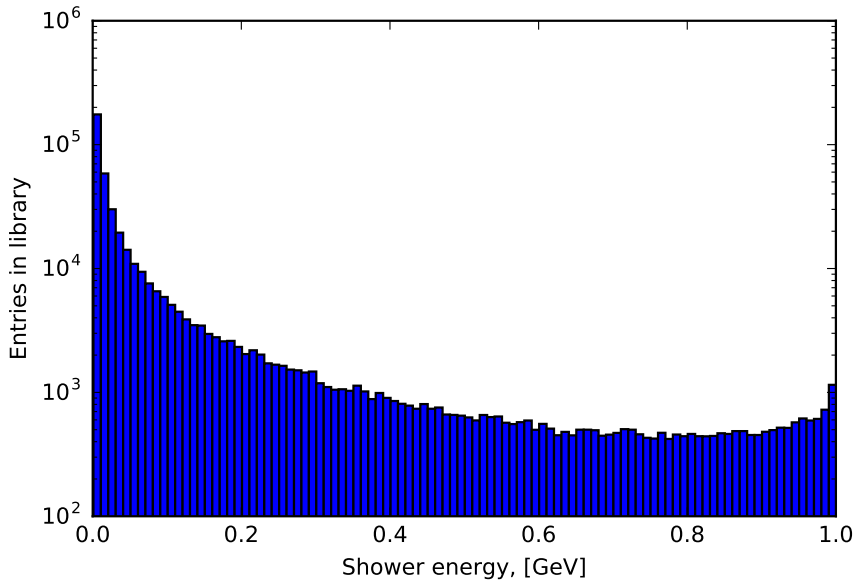


Fig. 8.7: Distribution of shower energy used in production of 1000 GeV electrons.

164 Unfortunately, for a Frozen Showers, generated for Run-1 monte-carlo, additional tuning of electron
 165 libraries was needed. This was done using reconstructed energy of electrons. Frozen Showers tend
 166 to underestimate fluctuations of energy loss, that is leading to a smaller electron resolution for a
 167 high energies. Correction is done by enlarging bin, corresponding to a gap position. Also, correction
 168 of the mean shift is done by scaling energy response of all showers. After this frozen showers are
 169 showing good agreement with full simulation. This procedure needs to be done every time, when
 170 something is changing in software. Because tuning is done manually, lots of manpower is needed
 171 for each Monte Carlo mass production campaign.

172 Distance binning problem

173 As it was mentioned before, process of library generation can be complicated and take a lot of the
 174 time because of the needed tuning. In this subchapter possible ways to improve frozen showers
 175 performance have been studied.

176 As it was mentioned before, that there are two type of material used in a FCAL. Showers within
 177 them are giving different response, what is affecting overall reconstructed electron energy resolution.
 178 At the first generations distance bin have been corresponding to LAr gap or dead material positions.
 179 During tuning bin with LAr was enlarged to gain a better agreement with full simulation. So, one of
 180 the basic ideas to improve frozen showers performance is to change a size of LAr gap in a library
 181 generation.

182 It was decided to treat showers, that have been born near LAr gap and crossed it on a radiation
 183 length, in a same way with showers in sensitive material gap, and call them sensitive material showers.
 184 Oppositely, showers, that haven't crossed LAr gap, are called dead showers. This model leads to a
 185 bigger gap width by a definition. One of the possible ways to find this bin position automatically is
 186 to use machine learning tools.

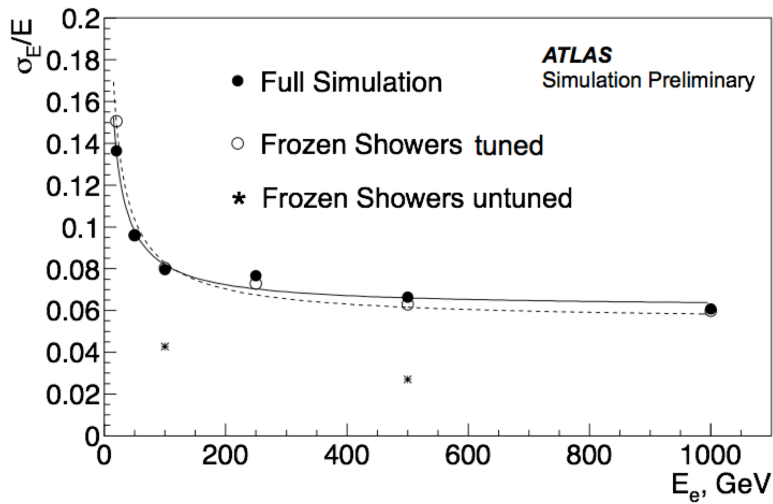


Fig. 8.8: Electron resolution for full simulation, tuned and untuned frozen showers

187 Machine Learning is a set of algorithms, what allows computers to learn and give a predictions
 188 without being specifically programmed. This is a modern field of computer science, that is wildly
 189 used in a different fields like computer vision, natural language processing, data science etc. There
 190 are two main types of machine learning algorithms: supervised, where example of desired output
 191 is given by the "teacher" and the goal is to learn a general rule, that maps inputs to outputs and
 192 unsupervised learning, then there are no labels given to algorithm, and algorithms is discovering
 193 hidden patterns in data. Initial data parameters of interest, that are used in algorithm to learn are
 194 called features. It is important to have right proper set of features and good training sample.

195 From a geometrical point of view, one of the main parameter is a direction of the shower. Eta
 196 momentum distribution is showed on a Figure 8.9 . Most of the showers are collinear to an electron
 197 direction. Because of this it was decided to use as a training sample simulation results for electrons
 198 with energies less than 1 GeV and momentum uniformly distributed between eta 3.0 and 4.0. This
 199 allowing to study equally low and high energy showers equally.

200 From our definition of 2 classes of showers, it is simple to construct a pre-labelled training sample.
 201 This is done by reducing initial sample and taking showers near rod center and inside liquid argon
 202 gap. Output of this classifier, that was trained on with sample with shower features, such as energy
 203 response and number of hits, than can be used to expand our labels to a full distance range. Then
 204 it can be used as an input to a second classifier, which will separate two types of showers using
 205 particle parameters, such as energy and distance to a rod center. For a first step decision trees have
 206 showed good classification efficiency (around 97%). For a second classifier support vector machines
 207 have been used. This method is trying to reconstruct a hyperplane, that is dividing two classes.
 208 Outputs of both of this classifiers are shown on a figure . New gap position is determined using
 209 borders of hyperplane. This procedure is giving expected from the initial model results. Gap is wider,
 210 than and original one. It is also getting bigger with bigger energy, because of the radiation length
 211 growth. Validation results for two different eta bins are shown on figure a) and b). In a bin this new
 212 binning is performing better, than original one without any additional tuning. Unfortunately this is not
 213 true for all of the bins, as we can see on a figure b). This eta bin have showed worst performance
 214 for a new binning, but it is performing still better, than original binning without tuning.

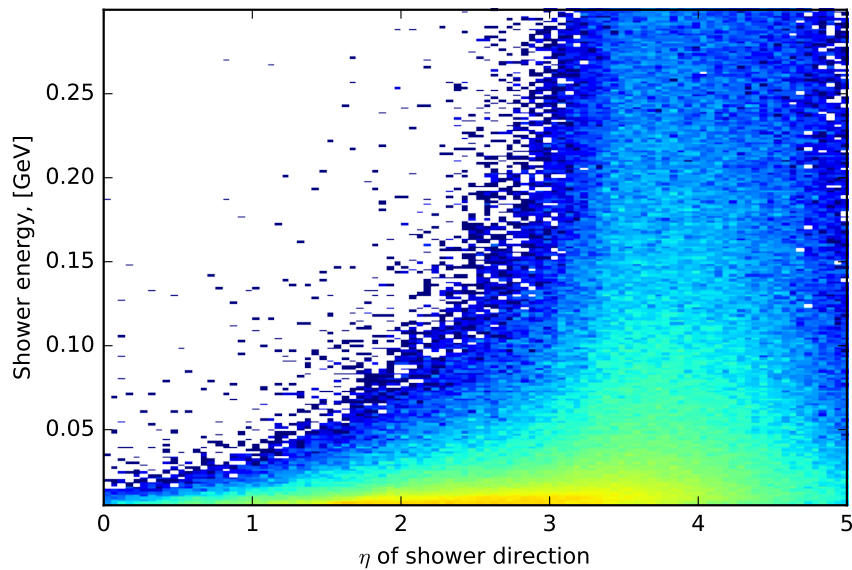


Fig. 8.9: Distribution of showers used in production of 1000 GeV electrons on shower energy vs $\eta_{momentum}$ plane.

215 This binning was used in a production of new libraries for Monte Carlo in a Run-2. It is planned to
216 use more precise training sample for a future iterations of this procedure for improving performance
217 of outlying eta bins.

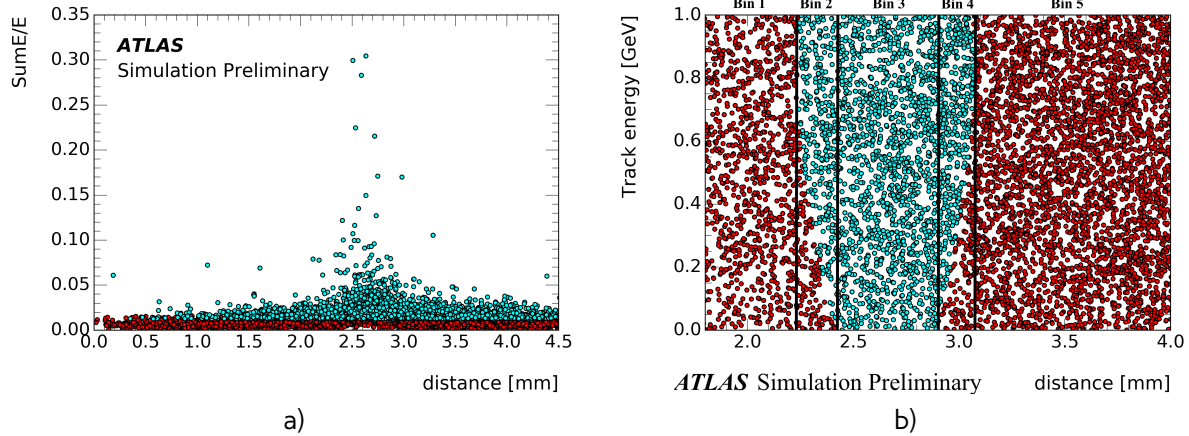


Fig. 8.10: Results of machine learning for a) first classifier b) second classifier. Cyan dots are corresponding to sensitive material showers, red - dead material showers

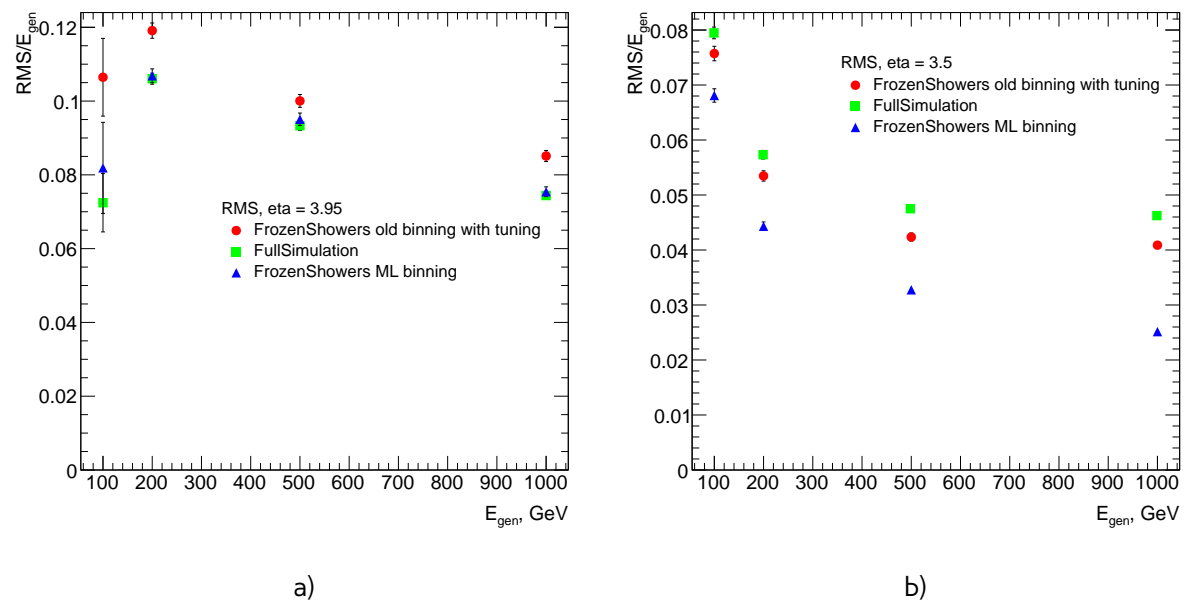


Fig. 8.11: Resolution of reconstructed electrons for full simulation, new libraries with ML binning and old tuned libraries with original binning for a) eta = 3.95 b) eta = 3.5

218

Chapter 9

219

DataSample

220

Part III

221

Measurement of cross-section

222 Chapter **10**

223 **Selection**

224 Selection criteria is the set of requirements, that is applied both on data and MC. Analysis is de-
225 pending on a selection, that can separate process of interest (signal) from other processes. For
226 $pp \rightarrow W \rightarrow ev/\mu\nu$ and $pp \rightarrow Z/\gamma^* \rightarrow ee/\mu\mu$ selection criteria can be divided into 3 groups: data
227 quality, lepton and boson cuts. In this chapter all of them will be discussed and a cut flow presented
228 In this chapter selection criteria for $pp \rightarrow W \rightarrow ev/\mu\nu$ and $pp \rightarrow Z/\gamma^* \rightarrow ee/\mu\mu$ are presented.

229 **10.1 Data quality cuts**

Table 10.1: Analysis selection

Event selection	
Single lepton trigger	
Good Run List	
Reject events with LAr errors	
Number of tracks at primary vertex ≥ 3	
Electron Selection	
$P_T > 20\text{GeV}$	$P_T > 20\text{GeV}$
$ \eta < 2.47$	$ \eta < 2.5$
excluding $1.37 < \eta < 1.52$	
OQ cut	staco reconstruction chain
Medium electron identification	Medium muon identification
$\text{PtCone}20 < 0.1$	$\text{PtCone}20 < 0.1$
W boson selection	
$\text{EtMiss} > 25 \text{ GeV}$	
$M_T > 45 \text{ GeV}$	$66 < M_{ee} < 116 \text{ GeV}$
Z boson selection	

230 For a measurement we must use the data with a proper quality. Unfortunately not all of the events
231 satisfy this criteria. One of the possible source of the problems could be that LHC was not in a
232 stable beam mode, or parts of the detector have been switched off, or event had too many noisy
233 cells. The information about luminosity blocks, that need to be excluded is stored in a "Good Run
234 List". Events, where LAr calorimeter was malfunctioning are excluded by LAr quality criteria. Events

235 are furthermore required to have at least one primary vertex from a hard scattering with at least 2
236 associated tracks reconstructed.

237 **10.2 Lepton quality cuts**

238 Online selection of events is based on a single lepton trigger, depending on a flavor of analysis.
239 For electron analysis it is required to have EF_e15_loose1 trigger, which records electrons with $E_T >$
240 7GeV . This trigger is also using additional "loose" isolation requirements to exclude jets, that are
241 misidentified as electrons. In muon channel lowest single lepton trigger available used (EF_mu10). It
242 records events with muons $E_T > 10\text{GeV}$. Moreover, matching between trigger and lepton is required.
243 All of the analysis are using similar selection criteria, applied on a leptons. All of the leptons must
244 satisfy requirement $P_T > 20\text{GeV}$ Electron candidates are required to be within pseudorapidity range
245 $|\eta| < 2.47$. Candidates within the transition region between the barrel and endcap electromagnetic
246 calorimeters, $1.37 < |\eta| < 1.52$, are removed. Additionally, for better multijet background rejection
247 medium identification and PtCone20 < 0.1 criterias are applied.

248 Muons are satisfying following criteria: they should be reconstructed by a staco algorithm in a
249 muon spectrometer and ... within range $|\eta| < 2.5$. Set of medium requirements is applied. They
250 must also satisfy PtCone20 < 0.1 isolation criteria

251 **10.3 Boson selection**

252 Events, contained W boson are required to have exactly one selected lepton. Events, where there are
253 additional "good" leptons are rejected. Missing transverse energy is required to be $E_{T\text{Miss}} > 25\text{GeV}$.
254 W boson, formed out of etMiss and lepton should have transverse mass $M_T > 45\text{GeV}$. After the
255 full selection total number of events in electron channel is ..(.. and .. for e^+ and e^- respectively.

256 The reconstructed lepton pair in case of Z boson analysis is required to invariant mass between
257 66 and 116 GeV. Both upper and bottom limits allows to exclude regions with high background
258 contamination and low statistics.

259 Full set of cuts is summarized in a table 10.1.

260

Chapter 11

261 Monte Carlo corrections

262 Monte Carlo plays important role in cross-section measurement. It is constantly undergoing correction
 263 to data, in order to obtain a required precision. Part of this corrections have been described in
 264 a chapter 8. Unfortunately, not everything can be taken into account during simulation itself. This
 265 leads to a differences between data and monte carlo, that needs to be accounted for. There are two
 266 possible methods to correct monte carlo without regenerating it. First on is to apply event weight, so
 267 what each mc event can contribute to non 1 entries in a histogram. This is called reweighting. Second
 268 one is to smear MC. It is using random number to alter reconstructed 4-vectors. This chapter de-
 269 scribes all additional corrections, what have been applied on MC in this analysis. All of this correction
 270 are introducing additional systematic error, that will be discussed in the chapter ??

271 11.1 Lepton efficiency corrections

272 Lepton detection efficiency at ATLAS detector can be divided into three components:

- 273 • The reconstruction efficiency ϵ_{rec} is a probability to reconstruct lepton as a lepton of this
 flavor.
- 275 • The identification efficiency $\epsilon_{id|rec}$ is the probability that a reconstructed lepton survives iden-
 tification requirements.
- 277 • The trigger efficiency $\epsilon_{trig|rec,id}$ is the probability, that lepton satisfy trigger requirements.

The full efficiency for a single lepton can be written as:

$$\epsilon_{total} = \epsilon_{rec} \times \epsilon_{id|rec} \times \epsilon_{trig|rec,id} \quad (11.1)$$

278 All of this efficiencies are measured using Tag and Probe method in $Z \rightarrow ll$ decays. This is allowing
 279 to insure, that all of the reconstructed lepton candidates are coming from an actual leptons. One of
 280 the leptons from Z boson, called "probe", is initially selected with all of the cuts, minus one under
 281 study. Second one, called "probe" satisfies more tighter selection with additional cut, such as, for
 282 example, trigger matching.

Reconstruction efficiency is assosiated with algorithm used to perform reconstruction. This is causing difference between electrons and muons efficiencies. In electron case it is a probability to reconstruct an elec tron with an electromagnetic calorimeter as an electron. Muon reconstruction efficiency is given by:

$$\epsilon_{reco,muon} = \epsilon_{reco,muon|ID} \cdot \epsilon_{ID} \approx \epsilon_{reco,muon|ID} \cdot \epsilon_{ID|MS}, \quad (11.2)$$

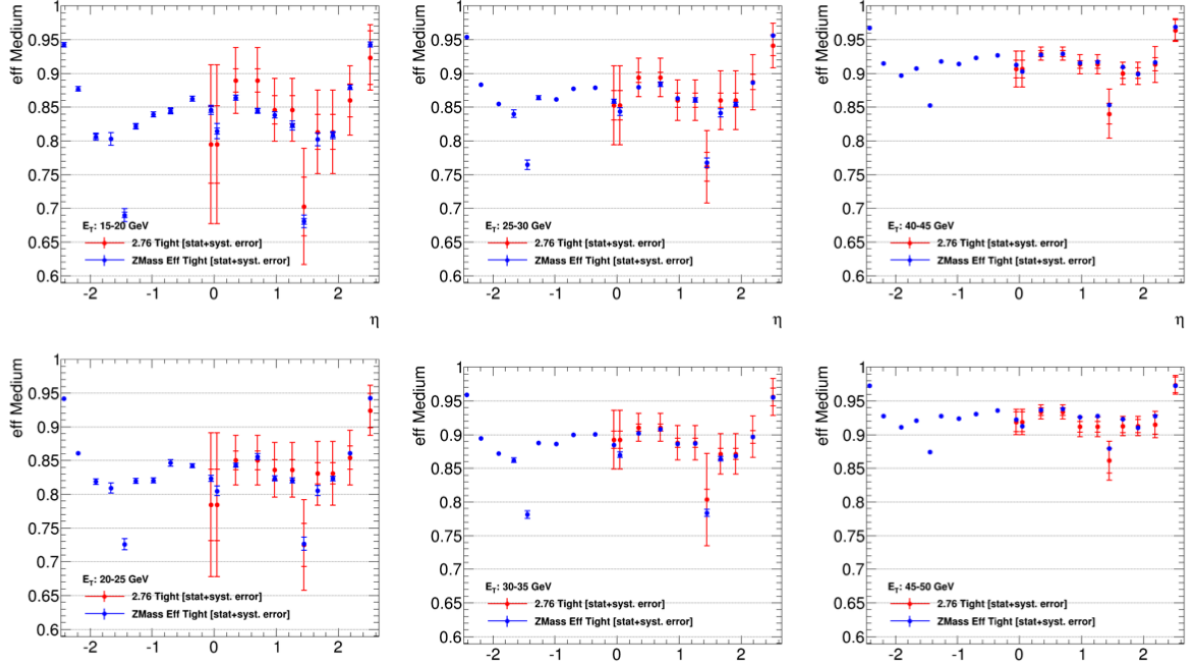


Fig. 11.1: Comparison of electron efficiencies as calculated for 8TeV (blue points) and 2.76TeV (red points) for MC simulation. Efficiencies are shown as a function of pseudorapidity (η) for different electron E_T bins. Both statistical and systematic uncertainties are shown.

where $\epsilon_{reco,muon|ID}$ is a conditional probability that muon reconstructed in ID is also reconstructed using MS as a combined muon, and ϵ_{ID} is a probability that muon is reconstructed as an ID track. This quantity cannot be measured directly and therefore is replaced by $\epsilon_{ID|MS}$, that can be measured by tag-and-probe method. uncertainty in this analysis.

Simulation samples are corrected to match data efficiencies by a scale-factor :

$$SF_{reco,id,trig} = \frac{\epsilon_{reco,id,trig}^{data}}{\epsilon_{reco,id,trig}^{MC}} \quad (11.3)$$

Each of the scale factors calculated in a p_t and η bins and has an associated statistical and systematical uncertainty component. Statistical component is connected to a size of $Z \rightarrow ll$, which is in our case is around 500 event per each lepton flavor. This means that precise calculation of scaling factors based on this data is difficult.

It is possible to use scale factors for 8 TeV 2012 data. The main difference between this data samples are center of mass energy and a pile-up conditions (10 in 2012 and less than 1 in 2013). This effects have been studied on a $Z \rightarrow ee$ sample. Fig. 11.1 shows that all of the differences in a scale factors are negligible and fully covered by the statistical error. This justifies the usage of 8 TeV scalling factors with increased

Unfortunately, single muon trigger haven't been presented in a 2012 data, so muon trigger scale factor needed to be derived from a 2.76 TeV data. Different configurations is calculated as a single number in order to minimize systematics contribution.

299 11.2 Electron energy scale and resolution

300 Electrons clusters tend to shift in a reconstructed energy compared to a truth energy of initial
 301 electron. Correction of this shift is done on a both data and MC as a 3 step process:

- 302 • Electronic calibration, that transfers a raw signal from a readout to a cluster energy deposit.
- 303 • MC based calibration. It corrects effects of energy loss in the material in front of calorimeter
 304 and leakage into the hadronic calorimeter. This calibration is applied on both data and MC.
- 305 • Correction of calorimeter cell responce in data. This is allowing to get right responce in non-
 306 optimal HV-regions and exclude biases in a calorimeter electronics reconstruction.

Energy shift is parameterised, as:

$$E^{data} = E^{MC}(1 + \alpha_i), \quad (11.4)$$

where E^{data} and E^{MC} are the energies in data and simulation, respectivelly and α_i is a mean shift in a given bin i in η . Effect of this miscalibration on a reconstructed mass of Z boson is:

$$m_{i,j}^{data} = m_{i,j}^{MC}(1 + \alpha_{i,j}), \quad \alpha_{i,j} \sim \frac{\alpha_i + \alpha_j}{2} \quad (11.5)$$

307 neglecting second order terms. $m_{i,j}^{data}$ and $m_{i,j}^{MC}$ are reconstructed mass of Z boson in a i and j bins
 308 of η for data and MC respectivelly.

There is also a need to correct difference in a electron resolution. It can be described by a formula
 8.1. It is assumed, that sampling and noise terms are moddeled well by MC and the main diiference
 is coming from a constant term. So, the electron resoultion correction then can be written as:

$$\frac{\sigma_E^{Data}}{E_i} = \frac{\sigma_E^{MC}}{E_i} \oplus c_i \quad (11.6)$$

309 where c_i is η dependent relative resolution correction. Similarly to a energy scale correction it is
 310 possible to derive resolution correction factor by a comparing $m_{i,j}^{data}$ and $m_{i,j}^{MC}$ distribution.

311 Correction values of α_i and c_i are obtained via χ^2 fit on a invariant mass electrons for data and
 312 MC. Resulting energy scale is applied on a data, while resolution is corrected for MC. The resulting
 313 scale is validated on a $J/\psi \rightarrow ee$ and $Z \rightarrow ee\gamma$

314 11.3 Muon momentum correction

Muon momentum resolution is depending on a η , ϕ and p_T of the muon [?]. There is an empirical formula to describe it inside the detector (ID or MS):

$$\frac{\sigma_{Det}(p_T)}{p_T} = \frac{r_0^{Det}(\eta, \phi)}{p_T} \oplus r_1^{Det}(\eta, \phi) \oplus r_2^{Det}(\eta, \phi) \cdot p_T \quad (11.7)$$

315 The first term origins from fluctuations of energy loss in transversed material. Second r_1^{Det} is com-
 316 ing from magnetic field inhomogenities and local displacements. Third term r_2^{Det} describes intrinsic
 317 resolution effects.

Similarly to electrons, overall energy scale shift between data and MC parameterised as:

$$p_T^{data} = p_T^{MC} + s_0^{Det}(\eta, \phi) + s_1^{Det}(\eta, \phi) \cdot p_T^{MC}, \quad (11.8)$$

where $s_0^{Det}(\eta, \phi)$ is coming from the imperfect knowledge of energy losses for muons passing through detector.

This leads to a total correction formula:

$$p_T^{Cor,Det} = \frac{p_T^{MC,Det} + \sum_{n=0}^1 s_n^{Det}(\eta, \phi) (p_T^{MC,Det})^n}{1 + \sum_{m=0}^2 \Delta r_m^{Det}(\eta, \phi) (p_T^{MC,Det})^{m-1} g_m}, \quad (11.9)$$

where g_m are normally distributed random variables with mean 0 and width 1. Because small amount of material between interaction point and the ID, $\Delta r_0^{ID}(\eta, \phi)$ and $s_0^{ID}(\eta, \phi)$ are set to 0. Missalignment effect for an MS is corrected on a simulation level by adding a random smearing to an alignment constants. This is allowing to set $\Delta r_2^{MS}(\eta, \phi)$ to 0 during a fit.

The correction factors are extracted using $Z \rightarrow \mu\mu$ candidates events with requirement on a two combined muons. For correction invariant mass distribution $m_{\mu\mu}^I D$ and $m_{\mu\mu}^{MS}$ are considered individually within a specific $\eta - \phi$ region of fit. Combined muon parameters are used to obtain angles η, ϕ . The correction extraction is performed first for an ID and then for MS with addition of the fit variable:

$$\rho = \frac{p_T^{MS} - p_T^{ID}}{p_T^{ID}}, \quad (11.10)$$

which represents p_T imbalance in ID and MS.

In a second step corrections are propagated to the combined momentum, using a weight average:

$$p_T^{Cor,CB} = f \cdot p_T^{Cor,ID} + (1 - f) \cdot p_T^{Cor,MS}, \quad (11.11)$$

where weight f is derived from mc.

326

Chapter 12

Missing Transverse Energy reconstruction and correction

329 Atlas detector has almost 4π coverage. This is allowing to calculate imbalance of energies inside
 330 calorimeter, especially transversal part of it called E_T^{miss} . Neutrino from a $W \rightarrow l\nu$ decay is leaving
 331 detector, without interacting with it, that is causing large energy imbalance in a detector.

Standard reconstruction of E_T^{miss} at ATLAS experiment uses transverse energy deposits in the calorimeter, energy losses in cryostat and reconstructed muons for a calculation:

$$E_{x(y)}^{miss} = E_{x(y)}^{miss,calo} + E_{x(y)}^{miss,cryo} + E_{x(y)}^{miss,muon}. \quad (12.1)$$

Calorimeter term is using information from reconstructed physics objects for calibration of cell response. The total transverse energy in calorimeter is defined as:

$$E_{x(y)}^{miss} = E_{x(y)}^{miss,e} + E_{x(y)}^{miss,\gamma} + E_{x(y)}^{miss,\tau} + E_{x(y)}^{miss,jets} + E_{x(y)}^{miss,SoftTerm} + E_{x(y)}^{miss,\mu}. \quad (12.2)$$

332 where each term is calculated as the negative sum of the calibrated reconstructed objects, projected
 333 onto the x and y directions. Each jet with energy $P_T > 20$ GeV is corrected for a pile-up and a jet
 334 energy scale is applied. Soft term is calculated from topoclusters and tracks, that are not associated
 335 with high-pt objects. To avoid double counting muon energy loss in calorimeter is subtracted
 336 from E_T^{miss} . The E_T^{miss} muon term is calculated from the momenta of muons measured in a range
 337 of pseudorapidity. Since pileup gives a significant effect on a E_T^{miss} performance several methods of
 338 pileup suppression are used. This procedure was optimised for 8 TeV runs and using a calibration
 339 constants from it. This can cause problems with 2.76 TeV low pileup run. As a examine showed this
 340 is not optimal procedure in this case. Control plots for W production in electron and muon channels
 341 are shown on a Fig. 12.3. Where a big discrepancies in a muon and electron channel, that cannot be
 342 accounted to multijet background.

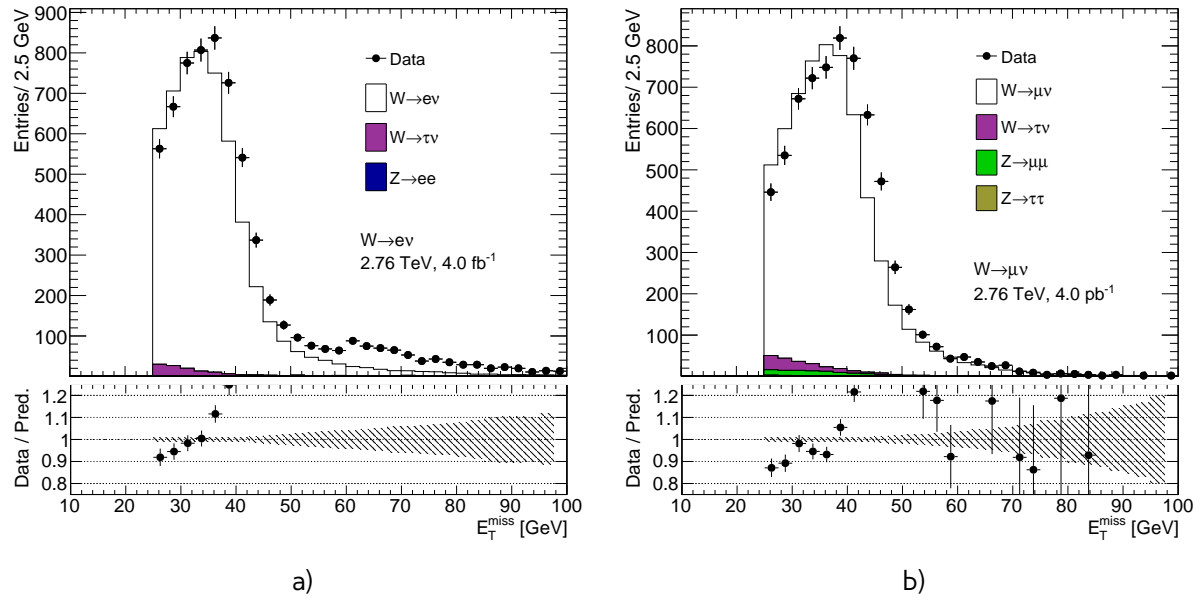


Fig. 12.1: Data and MC comparison for E_T^{miss} calculated by standard ATLAS algorithm for a) $W \rightarrow e\nu$ b) $W \rightarrow \mu\nu$ events

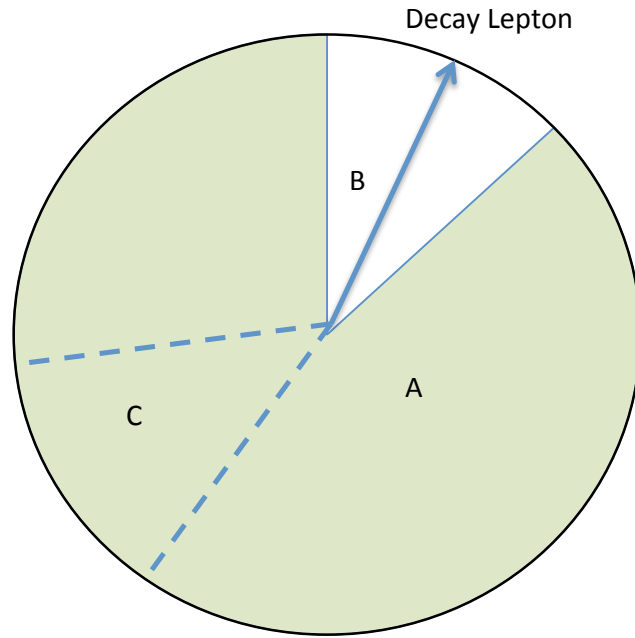


Fig. 12.2: Definition of different zones in the calculation of the cluster-based hadronic recoil.

343 12.1 Hadron Recoil Calculation

Second way of calculating E_T^{miss} was developed specifically for a W and Z decays by W mass measurements group. This procedure is using this fact, that a transverse momentum of a W-boson has to be balanced with initial (quark-gluon) state radiation, because initial sum of transverse momentum is zero:

$$\vec{P}_T^W = \vec{P}_T^{lep} + \vec{P}_T^\nu = \sum \vec{P}_T^{ISRquarks,gluon}, \quad (12.3)$$

where $\sum \vec{P}_T^{ISRquarks,gluon}$ is a transverse momentum of partons from initial state radiation, also called hadronic recoil (HR). Therefore, E_T^{miss} can be determined as:

$$E_T^{miss} = P_T^\nu = -HR + p_T^l \quad (12.4)$$

This procedure assumes, that recoil is arises from one single leading jet, and the rest is coming from a soft hadronic activity. This hadron recoil is computed as a vector sum of calorimeter clusters:

$$HR = \sum_{i=0}^{N_{topo}} \vec{p}_T^{topo} \quad (12.5)$$

while a scalar sum of all transverse energies is corresponding to the hadronic activity of the event:

$$\sum E_T = \sum_{i=0}^{N_{topo}} E_T^{topo} \quad (12.6)$$

344 To avoid double counting of lepton energy losses in calorimeter, the clusters inside cone with radius
 345 $dR = 0.2$ are excluded from this calculation. To compensate soft activity inside this cone, clusters
 346 are then compensated by replacement cone (Fig. 12.2). This cone is defined as cone at the same
 347 pseudorapidity, but different ϕ . It should be far from any other lepton and hadron recoil direction.
 348 Each cone is then rotated to a direction of the original lepton direction. This definition is not taking
 349 into account jet reconstruction aspects. This is allowing to get a better data MC agreement (Fig. ??).

350 where \vec{v} is the unit vector along boson p_T direction. Parallel component is sensitive to a bias
 351 relative to a truth P_T^W of the boson, while perpendicular component is 0 on average and affected
 352 just by a resolution effects. Momentum of Z boson can be precisely determined by a measurement
 353 of its decay products. This is allowing to determine data driven hadron recoil corrections. Due to a
 354 low cross-section of Z production, these corrections are mostly statistically dominated. On another
 355 hand, it is also possible to use W boson decays for a not so systematically precise, but statistically
 356 better.

357 However, due to a limited statistics of a Z decays in this data, it is better to combine this with a
 358 corrections derived from W decays da

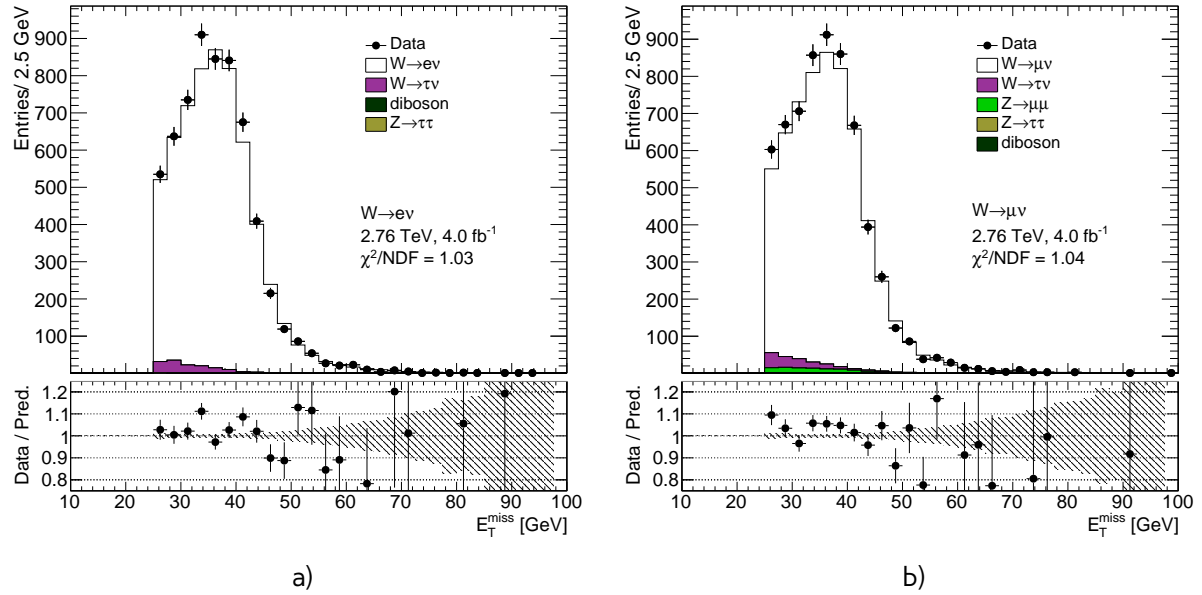


Fig. 12.3: Data and MC comparison for E_T^{miss} calculated from hadron recoil for a) $W \rightarrow e\nu$ b) $W \rightarrow \mu\nu$ events

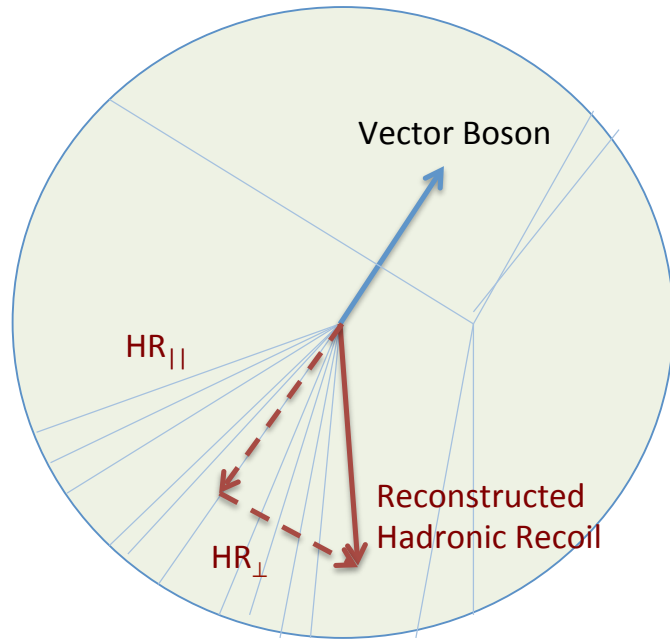


Fig. 12.4: Parallel and perpendicular projection of the hadronic recoil with respect to the transverse momentum of the vector boson

359 12.2 Hadron Recoil calibration

360 E_T^{miss} affects significantly on a W boson measurement, so its important to have good understanding
 361 of sources of a possible differences in a hadron recoil reconstruction in a data and monte carlo.

This differences can be paramerised at the respect of the truth boson Pt as follows:

,

(12.7)

362 where $u_{||}$ is a projection to the direction of the truth boson pt, and u_{\perp} is the projection on a
 363 perpendicular plane. On average $u_{||}$ should be match absolute value of boson pt and thus this
 364 quantity is sensitive to a relative bias of hadron recoil reconstruction. On another hand u_{\perp} comes
 365 from calorimeter resolution and should have 0 mean. This component is sensitive to a discrepancies
 366 in data/mc resolutions.

367 Standard procedure of calibrating hadron recoil uses Z boson, since its transverse momentum can
 368 be determined not only by a hadron recoil, but also from its decay products. Zpt resolution coming
 369 from lepton reconstruction is around 10 GeV, while hadron recoi resolution is around 30 GeV, what
 370 is alowing to have a precise determination of a calibration constants. On another hand, size of the
 371 Z sample in 2.76 TeV data is small, so this constants will be statistically dominated.

372 On another hand, in W decays hadron recoil corrections cannot be determined through boson
 373 pt directly, but this channel has a better statistics. The procedure is more complicated, because it
 374 should not change truth boson spectrum and not correct additionally boson pt mismodelling.

375 At the end, the combination of 2 determination results have been used. This section describes a
 376 procedure of calibrating bias and resolution mismodelling in a hadron recoil, that was apapted for
 377 2.76 TeV data.

378 12.2.1 Underlying event mismodelling correction

379 One of the possible sources of diffetences in data and MC is a modelling of underlying event. Soft
 380 interactions cannot be computed precisely by a pertrubative quantum chromodynamics methods, so
 381 it is usually described by a phenomenological models, that can be not so precise. Pile-up mismodelling
 382 usually accounted by correcting average number of interaction per bunch crossing to match a data.
 383 However, ATLAS simulation is suited for an ordinary high pile-up runs, so this quantity is not modelled
 384 well in a case of 2.76 TeV analysis ??.

385 Another quantity that depends on a underlying event is a $\sum E_T$, defined in a Eq. 12.6. There is a
 386 visible shift between data and monte carlo in a both channels. This is causing differences in a hadron
 387 recoil resolution, since this variables are highly correlated (add some figure). Size of the Z sample is
 388 not sufficient to determine the correction factors, so the W boson was used.

To leave boson pt spectrum untouched, correction factors are determined inside pt bins as:

$$SF^{channel} = \frac{\sum E_T^{data}(p_T^{W,rec})}{\sum E_T^{MC,channel}(p_T^{W,rec})}, \quad (12.8)$$

389 where $\sum E_T^{data}(p_T^{W,rec})$ and $\sum E_T^{MC,channel}(p_T^{W,rec})$ are a $\sum E_T$ distributions inside $p_T^{W,rec}$ for data and
 390 monte carlo respectively. Scale factors are determined separately for each signal process. In order
 391 to increase statistics in data the combination of $W \rightarrow e\nu$ and $W \rightarrow \mu\nu$ processes is used. Example
 392 of this correction factors for $W^+ \rightarrow e\nu$ is shown on a Fig. ??.

393 The distribution of $\sum E_T$ after correction is shown on a Fig. ?? Reconstructed and truth boson
 394 spectrum is staying untouched (Fig.). Systematic error coming from this method can be studied by

parametrisation of scale factors with polynomial order 2 inside each $p_T^{W,rec}$ bin. Statistical uncertainty correction can be determined through the uncertainties of this approximations. Set of the scale factors with polynomial parametrisation have been produced. For each scale factor inside this set polynomial parameters have been varied inside its unsertanty (correlation between parameters have been taken into accound). Systematical errors can be determined by using additional parametrisation of scale factor inside the bin with polynomial. The overall effect on a C_W for a different methods is shown in a Tab. ???. As it can be seen, sign of the effect is different for electron and muon flavor of the analysis.

12.2.2 Hadron recoil bias correction

As it was mentioned before, it is possible to use both Z and W boson sample for hadron recoil bias determination. Correction factor $SF_{HR,bias}$ is applied as:

$$u_{\parallel}^{MC,cor} = u_{\parallel}^{MC} \cdot SF_{HR,bias}, \quad (12.9)$$

and can be obtained by scanning the impact of the scaling factor on the Data to MC agreement of the distributions that are dominated by the recoil scale uncertainties. Since W boson has no second source of P_T^W measurements, determination of the hadron recoil bias should use the distributions, that are not sensitive to a truth P_T^W spectrum. One of the optimal choises is a M_T^W distribution. Transverse mass distribution for a different scale choises is shown on a Fig. ???. Multijet background is not included, because it shape and number of events is depending on a hadron recoil scale and thus can introduce additional systematics.

The first way to determine correction factor is using a difference in the mean of transverse mass in data and MC. Statistical error of this determination is an error of the mean in the data. The precision of this method is low, is it is mainly used as a cross-check.

Second way is calculating χ^2 for each correction factor. The ideal correction factor is determined by fitting χ^2 distribution by the function:

$$\chi^2 = \frac{(x - sf_{best})^2}{\sigma_{sf}^2} + \chi_0^2, \quad (12.10)$$

where sf_{best} is the best scale factor and σ_{sf} is a statistical error of this parameter. Distribution of χ^2 and a fit in combined W channel is shown on a Fig. ???.

Because of the possible mismodelling of the tail M_T^W distribution it is not included in a χ^2 calculation, leaving a free choise of the parameter of the cutoff. It is also possible to exclude regions with high multijet background contamination by applying a tighter cut on a M_T^W . This fit range is introducing one source of systematic error. Effect of the range on value determination is shown on a Fig. ???. Similarly to a W channel, scale correction in a Z sample can be determined from distribution $\frac{u_{\parallel}}{p_T^{\parallel}}$, shown on a Fig. ???. Since there is no choise of the range and dependency on P_T^{bos} modelling, there is just one source of uncertainty.

Results on a hadron scale factros and it's errors are shown in a Table ???. The results are consistent within 1 sigma. Overall effect on a C_W is shown on a Tab. ???.

12.2.3 Hadron recoil resolution correction

426

Chapter 13

Background estimation

428 After the event selection described in chapter 10 the background contribution is around % for W
 429 and % for Z analysis (which is with this statistics is negligible). Main backgrounds for W analysis
 430 are coming from:

- 431 • Processes with τ lepton, misidentified as a electron or muon + missing energy from neutrino
 432 • Z decays with one missing lepton.
 433 • QCD processes. In electron channel this is mostly coming from jets faking electrons, while in a
 434 muon channel it consists mostly of a real muons produced in decays of heavy-flavor mesons.

435 Most of the backgrounds are estimated using MC. They are normalized using highest cross-section
 436 order available. The total list of simulated backgrounds and its cross-section is shown in a Table 13.1.
 437 QCD background is estimated using data driven method.

Table 13.1: Background processes with their associated cross sections and uncertainties. The quoted cross sections are used to normalise estimates of expected number of events

Process	$\sigma \cdot BR$ [pb]	Order
$W^+ \rightarrow l\nu$	2116(1.9)	NNLO
$W^- \rightarrow l\nu$	1267(1.0)	NNLO
$Z \rightarrow ll$	303(0.2)	NNLO
$t\bar{t}$	7.41	LO
WW	0.6	LO
ZZ	0.7	LO
WZ	0.2	LO
$DY \rightarrow ee$	2971	LO
$DY \rightarrow \mu\mu$	2971	LO

13.1 QCD background estimation

438 There is a small probability, that jet can fake W-boson decay with isolated lepton and E_T^{miss} through
 439 the energy mismeasurement in the event. Event selection is suppressing this type of the background,
 440 but not fully eliminating it. Due to a large jet production cross-section and complex composition,

442 generation of MC events becomes impractical. This is why data driven technique for QCD back-
 443 ground estimation have been used. In our case contribution of the QCD background in a Z sample
 444 is negligible, so it is estimated just for a $W \rightarrow e\nu$ and $W \rightarrow \mu\nu$ processes.

445 Data driven method allows to have model independent predictions with small statistical uncertainty.
 446 This method is using *QCD* enriched region, where signal events are suppressed. This is usually done
 447 by reversing identification or isolation criteria. It is assumed, that shape of the qcd background is
 448 staying the same in the signal region. Normalization can be derived in a control region through the
 449 template fit.

450 This section describes method of QCD background determination, that have been used in 2.76
 451 TeV data.

452 13.2 Template selection

A study have been performed to determine appropriate template selection. Identification criteria are inverted in order to suppress the signal events. Because of the origins of the QCD backgrounds, missing transverse energy E_T^{miss} should be smaller in a QCD, than in a signal region. Releasing E_T^{miss} cut is allowing to gain a bigger statistics for a QCD template. The template sample can have a contributions from other backgrounds (mostly coming from $W \rightarrow l\nu$). In order to avoid double counting, they are subtracted from a template. The total number of events in the template can be defined as:

$$N_{template} = N_{data}^{bkg\ enriched} - \sum_j^{MC} N_{MC_j}^{bkg\ enriched}, \quad (13.1)$$

453 where $N_{data}^{bkg\ enriched}$ and $N_{MC_j}^{bkg\ enriched}$ are number of the events in a background enriched sample in data
 454 and MC respectively.

455 For electron flavour, template is build by requiring the electron candidate to fail Medium isolation
 456 criteria, but to pass loose selection. The resulting shape of the QCD background is shown on a Fig.
 457 ???. Events are selected to pass looser trigger <>, which requires on electron candidate that passing
 458 $p_T^{lep} > 10$ GeV and loose ID criteria. The total number of events in a templates is <somethig>. The
 459 stability of the template can be studied by reversing different identification criteria. As it can be
 460 seen on a Fig. ???, ID criteria is almost not affecting shape of the QCD background.

461 It is impossible to use similar procedure in muon channel, since the resulting statistics of template
 462 is small (Fig. ??). Another way of defining QCD template is using the properties of the process, that
 463 is resulting in a fake muons. Fake muon are mostly coming from a heavy flavour decays. If a charged
 464 hadron comes through the HCAL, it can leave a track in MS and be identified as a muon. Most of
 465 the time there are multiple tracks in the ID. So the template muon is selected as a muon, that has
 466 track in the ID, but has no track in MS. Effect on the shape of this selection can be studied using
 467 smaller sample of $b\bar{b}$ and $c\bar{c}$ MC samples. Additionally, checks on a differences in a shape between
 468 signal and template region have been performed (Fig. ??). This is totally justifies this choice of the
 469 template selection. Shape of the background should not depend on the charge of the analysis, so it
 470 was decided to use template, combined in a both channel. The resulting template is shown on a Fig.
 471 ???. Total number of events in a template <something>.

472 13.3 Methodology of the template sample normalization

As it was mentioned before, multijet events tend to have smaller E_T^{miss} , than a signal. It was desided to use E_T^{miss} distribution with the released E_T^{miss} cut for a finding a template shape normalization. The normalisation is found through the χ^2 fit of the template and backgrounds to the data. The following composite model have been used for estimation:

$$M(E_T^{miss}) = \sum_{i=1}^{N-1} f_i F_i(E_T^{miss}) + (1 - \sum_{i=1}^{N-1} f_i) \cdot F_{qcd}(E_T^{miss}), \quad (13.2)$$

473 where $F_i(E_T^{miss})$ and $F_{qcd}(E_T^{miss})$ are the probability density functions of MC samples and QCD back-
474 ground template respectively. Fit parameters f_i are the fractions of MC within fit region. In order
475 to eliminate systematics, coming from cross-section uncertainty, with signal fractions are left freely
476 and and background MC fractions are varied within 5% uncertainty.

Normalisation scale for QCD events is calculated from obtained fit parameters as:

$$scale = \frac{(1 - \sum f_i) \cdot N_{Data}^{fit}}{N_{template}}, \quad (13.3)$$

477 where $\sum f_i$ is a sum of all fractions in the fit, N_{Data}^{fit} is a number of data events in a fit histogram
478 and $N_{template}$ is a number of event in a template. The fit is performed separately for W^+ and W^- .
479 Additionally, fit in uncharged W channel is used as a cross-check of the fit. The results of the fitting
480 procedure are shown on a Fig. . Total number of events and fit uncertainty are shown in a Tab. ??.
481 The overall fraction of QCD events is lower, than in 7 TeV data <reference to a 7 TeV paper>, what
482 is agreeing with expectations.

483 13.4 Systematic Uncertainty from the Multi-jet Background 484 Estimation

The uncertainty of multi-jet background can esimation can be divided into 3 main components:

$$\delta_{QCD} = \sqrt{\delta_{fit\,unc} + \delta_{fit\,bias} + \delta_{template}}, \quad (13.4)$$

485 where $\delta_{fit\,unc}$ is the uncertainty for a scale from a χ^2 fit. The second $\delta_{fit\,bias}$ is coming from an effect
486 from arbitrary choise of binning and fit range. This error is estimated by repeating fit for a different
487 bin and range choises. Fird uncertainty is due to a potential bias in the template as a result of the
488 template choise and a template statistics itself.

489

Chapter 14

490 Uncertainties

491 **14.1 Toy MC method**

492 **14.2 Experimental systematic uncertainties**

493 table about methods

494 **14.2.1 Hadron Recoil correction uncertainty**

495 **14.3 Theoretical uncertainty**

496 • PDF

497 • Parton shower and matrix element

498

Chapter 15

499 **Control distributions**

500

Chapter 16

501 **Results of the Cross Section Measurement**

502 **16.1 Cross-Section measurement definition**

503 **16.2 Fiducial phase-space**

504 **16.3 Comparation with Theoretical Predictions**

505

Part IV

506

PDF fits

